

**Dynamical triplet unraveling : A quantum Monte Carlo algorithm for reversible dynamics**

Romain Chessex <sup>\*</sup>, Massimo Borrelli, and Hans Christian Öttinger   
*Polymer Physics, Department of Materials, ETH Zürich, CH-8093 Zürich, Switzerland*

 (Received 22 June 2022; accepted 23 August 2022; published 31 August 2022)

We introduce a quantum Monte Carlo method to simulate the reversible dynamics of correlated many-body systems. Our method is based on the Laplace transform of the time-evolution operator, which, as opposed to most quantum Monte Carlo methods, makes it possible to access the dynamics at longer times. The Monte Carlo trajectories are realized through a piecewise stochastic-deterministic reversible evolution where free dynamics is interspersed with two-process quantum jumps. The dynamical sign problem is bypassed via the so-called *deadweight approximation*, which stabilizes the many-body phases at longer times. We benchmark our method by simulating spin excitation propagation in the one-dimensional (1D) XXZ spin chain, dynamical confinement in the 1D quantum Ising model and quenched magnetization dynamics in the two-dimensional square Ising model. Finally, we also show how to extract dynamical information directly from the Laplace representation.

DOI: [10.1103/PhysRevA.106.022222](https://doi.org/10.1103/PhysRevA.106.022222)

**I. INTRODUCTION**

Recent years have witnessed an ever-growing interest in the many-body dynamics of strongly correlated quantum systems [1,2]. Technical advancements in quantum state preparation, control, and measurement have made it possible to observe the real-time evolution of typical systems in condensed matter physics at very low temperatures. Several experimental platforms, ranging from cold atoms in optical lattices [3–7] to trapped ions [8,9] and superconducting circuits [10,11], have emerged as quantum simulators and different many-body Hamiltonians have been realized. The plethora of phenomena that were investigated is very rich and includes many-body equilibration versus localization [12–14], many-body dissipation, dynamics of quantum correlations [15–17], quenched many-body dynamics, and dynamical phase transitions [18–20].

Parallel to the abundance of experimental investigations, numerical methods [19,21,22] were developed to simulate condensed matter systems efficiently, including molecular and atomic gases in optical lattices. At the intersection between many-body physics and quantum information theory, tensor networks were extensively explored in one-dimensional (1D) systems, and nowadays, they are considered as a universal representation of low-energy, weakly entangled quantum states. Within this framework, time-dependent density matrix renormalization group [23–26] has proven very effective in handling large particle systems and has established itself as a reliable standard tool. For higher-dimensional systems and longer simulation times, nonequilibrium dynamical mean-field theory [27,28] has been successfully applied to study spectroscopy [29], nonlinear optics [30], and transport in solid-state physics [31] as well as quenches [32] and relaxation dynamics in cold atoms in optical lattices [33,34].

Finally, other computationally efficient methods found a multitude of applications in quantum chemistry, with prominent examples being the time-dependent Hartree-Fock [35], multi-configurational time-dependent Hartree-Fock [36], in which some electron-electron correlations are also included, and density functional theory [37].

Most of the above techniques rely explicitly on symmetries in the Hamiltonian to cope with the large size of the Hilbert space. As opposed to deterministic techniques, quantum Monte Carlo methods (QMC) sample stochastic trajectories in a configuration space, onto which the original Hilbert space is directly mapped, and proved very reliable in a number of different applications [38–43]. Although QMC methods were originally formulated to study ground-state and equilibrium properties, dynamical adaptations have also been put forward that are based on stochastic sampling of diagrammatic expansions of many-body Green's functions defined along a Keldysh contour [40,44,45]. All these methods, however, were limited in accessing long-time behavior by the well-known dynamical sign problem. Notable exceptions were the inchworm algorithm presented in [46] and real-time full configuration interaction QMC algorithm [39]. The first technique can access medium-to-long-time  $t \sim 10$  dynamical properties due to corrections of short-time diagrams, whereas the second can allow for simulation times up to  $t \sim 40$ , although at the expense of probability conservation.

Here, we present a QMC algorithm that allows us to simulate the reversible dynamics of a quantum many-body system at long times. In some technical aspects, this method draws from the fixed point quantum Monte Carlo method (FPQMC), which was first introduced in [47] for ground-state calculations. The reversible dynamics, as dictated by the von Neumann equation, is reformulated in the Laplace representation and unraveled by stochastic trajectories. These are generated by a piecewise deterministic-stochastic evolution where the free part of the many-body Hamiltonian is solved exactly, while particle-particle interactions are

<sup>\*</sup>rchessex@ethz.ch

simulated using two-process quantum jumps. The QMC walkers sampling the configuration space are called triplets and consist of two state vectors and a statistical weight. Depending on this weight, a triplet might spawn a new triplet via a two-process quantum jump or be removed from the simulation altogether. Two key ingredients are introduced. First, the *deadweight approximation*, which stabilizes the phases originating from fast oscillating exponentials that are responsible for the dynamical sign problem. Second, as previously formulated in FPQMC and relying on the *dynamic norm*, importance sampling guarantees fast convergence of the time-dependent quantities under scrutiny. Near-exact trace conservation of the density matrix is guaranteed for the entire duration of the simulation. We benchmark our algorithm against three case-studies on quantum lattices: (i) dynamics of a spin excitation following a quench in the 1D Heisenberg XXZ chain; (ii) excitation confinement in the 1D quantum Ising model [48–50]; and (iii) dynamics of magnetization following a quench in the two-dimensional (2D) Ising mode. In all three cases we find results in excellent agreement with previously established literature whenever a comparison is possible.

This paper is organized as follows. In Sec. II, we present the theoretical background for our numerical method and introduce some physical quantities of interest. In Sec. III, we break down the algorithm itself and explain in detail all its major components. In Sec. IV, we test our method for the case studies mentioned earlier and analyze the results. Finally, we draw some conclusions and illustrate some open perspectives in Sec. V.

## II. THEORETICAL BASIS

### A. Dynamics in the Laplace space

We focus on many-body systems whose Hamiltonian  $H$  can be split into a free part and an interacting part, that is,  $H = H^{\text{free}} + H^{\text{int}}$ . The adjectives “free” and “interacting” do not necessarily refer to the actual kinetic energy versus interactions within the Hamiltonian, but rather to whether the exact eigenstates are known *a priori*, which is assumed to be always the case for  $H^{\text{free}}$ . The time evolution is dictated by the *von Neumann* equation

$$\frac{d}{dt}\rho = \mathcal{L}\rho \equiv -i[H, \rho], \quad (1)$$

where  $[\cdot, \cdot]$  denotes the commutator and  $\rho$  the density matrix of the many-body system. If the total Hamiltonian is time independent, the formal solution of Eq. (1) reads

$$\rho_t = \mathcal{E}_t \rho_0 = e^{t\mathcal{L}} \rho_0, \quad (2)$$

for some initial state  $\rho_0$ . To use the framework developed in [47], we transform the time-evolution superoperator  $\mathcal{E}_t$  in the Laplace domain, that is,

$$\mathcal{R}_s = \int_0^\infty \mathcal{E}_t e^{-st} dt. \quad (3)$$

We define the superoperators

$$\mathcal{L}^{\text{free}}\rho = -i[H^{\text{free}}, \rho], \quad \mathcal{L}^{\text{int}}\rho = -i[H^{\text{int}}, \rho], \quad (4)$$

generating the dynamics described by the superoperators  $\mathcal{R}_s^{\text{free}}$  and  $\mathcal{R}_s^{\text{int}}$ , respectively. By first Laplace-transforming the for-

mal solution of Eq. (1) and then applying the geometric series (see [51] for details), one arrives at the following expression for the Laplace transform of the total evolution superoperator  $\mathcal{R}_s$ :

$$\mathcal{R}_s = \sum_{m=0}^{\infty} r^m \left[ \mathcal{R}_{s+r}^{\text{free}} \left( 1 + \frac{\mathcal{L}^{\text{int}}}{r} \right) \right]^m \mathcal{R}_{s+r}^{\text{free}}, \quad (5)$$

with  $r > 0$ . We refer to Eq. (5) as the *magical formula* because it unifies a perturbative expansion and a numerical scheme in a single equation. If  $r = 0$ , the perturbative expansion is recovered, since the  $m$ th term in the sum corresponds to the  $m$ th order in perturbation theory. Conversely, if  $r > 0$ , the sum can be interpreted as the time-evolution operator of a numerical integration scheme with a  $1/r$  time step. Hence, truncating the magical formula at some  $M_{\text{trunc}}$  term sets a natural time limit for the numerical integration, which is  $t_{\text{max}} \sim \frac{1}{s_{\text{min}}} \sim \frac{M_{\text{trunc}}}{r}$ .

The Laplace transform of the time-evolution superoperator (3) does not guarantee trace conservation by itself. However, noting that

$$\text{Tr}(\mathcal{R}_s \rho_0) = \int_0^\infty \text{Tr}(\rho_t) e^{-st} dt = \frac{1}{s}, \quad (6)$$

we recover the correct normalization for the quantity  $\tilde{\rho}_s$  defined by

$$\tilde{\rho}_s = s \mathcal{R}_s \rho_0. \quad (7)$$

Even though  $\tilde{\rho}_s$  possess all properties of a density matrix, we have to be careful when interpreting it as a physical density matrix because it is constructed from an integration over the entire time domain. In the limit  $s \rightarrow \infty$ , the density matrix is associated to a physical state, however, for any finite value  $s$ ,  $\tilde{\rho}_s$  can be interpreted only as a formal density matrix.

Once the density matrix  $\tilde{\rho}_s$  is obtained, relevant quantities of interest can be calculated. For instance, the  $s$ -dependent correlation functions read

$$C_s^{AB} = \text{Tr}(AB\tilde{\rho}_s) = s \text{Tr}(AB\mathcal{R}_s \rho_0), \quad (8)$$

where  $A$  and  $B$  are generic self-adjoint operators.

### B. Two-process stochastic unravelling

As mentioned earlier, the magical formula (5) can be interpreted as an integration scheme for any  $r > 0$ . In this respect, the superoperator

$$T_r(s) = r \left[ \mathcal{R}_{s+r}^{\text{free}} \left( 1 + \frac{\mathcal{L}^{\text{int}}}{r} \right) \right], \quad (9)$$

should be regarded as the fundamental propagator in the Laplace domain. As anticipated earlier, a truncation order  $M_{\text{trunc}}$  is set in the numerical implementation, which leads to the following approximation of the evolution superoperator

$$\mathcal{R}_s \approx \sum_{m=0}^{M_{\text{trunc}}} [T_r(s)]^m \mathcal{R}_{s+r}^{\text{free}}. \quad (10)$$

From this approximation, we develop a stochastic process to unravel the von Neumann equation. We take inspiration from the method originally introduced as *triplet unravelling* in [47]. Our method tracks the evolution of Monte Carlo walkers, called triplets, of the form  $(c_m, |\phi_m\rangle, |\psi_m\rangle)$  in the

many-body Hilbert space where the subscript  $m$  refers to the  $m$ th-order iterative term in the evolution described by the propagator (9). The evolution of the piecewise-deterministic stochastic processes  $|\phi_m\rangle, |\psi_m\rangle$  alternates between an exact continuous evolution, governed by  $H^{\text{free}}$ , and stochastic state jumps accounting for  $H^{\text{int}}$ . We construct these processes as to reproduce the application of the magical formula Eq. (5) for infinite order of iteration  $M_{\text{trunc}} \rightarrow \infty$  via

$$\tilde{\rho}_s = s \sum_{m=0}^{\infty} \mathbb{E}[c_m |\phi_m\rangle \langle \psi_m|], \quad (11)$$

where  $\mathbb{E}[\cdot]$  represents the expectation value of the stochastic processes. This construction ensures that the solution of the von Neumann equation in the Laplace domain is recovered in the limit of a large order of iteration. Because eigenstates of  $H^{\text{free}}$  are assumed to be known exactly, we use these states as the computational basis allowing us to compute the free evolution exactly. To minimize the statistical correlations between the processes  $|\phi_m\rangle$  and  $|\psi_m\rangle$ , we use two-sided jump processes and model the effect of  $H^{\text{int}}$  as follows:

$$|\phi_m\rangle \langle \psi_m| \mapsto |\phi_m\rangle \langle \psi_m| - \frac{i}{r} (H^{\text{int}} |\phi_m\rangle \langle \psi_m| - |\phi_m\rangle \langle \psi_m| H^{\text{int}}), \quad (12)$$

which coincides with a stochastic application of the superoperator  $(1 + \frac{L^{\text{int}}}{r})$ .

### III. DYNAMIC ALGORITHM

The present algorithm is the dynamical adaptation of the FPQMC method introduced in [47], of which it preserves the overall structure. This structure consists of a main loop whose application is iterated over an ensemble of triplets until a solution emerges. Two distinct steps compose the main loop, the *interaction* and the *free evolution* that are implemented by the superoperators  $(1 + \frac{L^{\text{int}}}{r})$  and  $\mathcal{R}_{s+r}^{\text{free}}$ , respectively.

#### A. Main loop

The algorithm considers the evolution of an ensemble of triplets, defined as  $\{(w_n, |i_n\rangle, |j_n\rangle)\}_n$ , where  $w_n$  is the (complex) weight factor and  $|i_n\rangle, |j_n\rangle$  are the free Hamiltonian eigenstates. Here the subscript  $n$  refers to the index in the triplet ensemble. In what follows, we will use the lighter notation  $|i\rangle \equiv |i_n\rangle$ . As anticipated earlier, during the evolution, the triplets repeatedly experience stochastic spawning events, realized by state jumps associated with  $H^{\text{int}}$ , interspersed with continuous weight updates coming from the exact, free evolution  $H^{\text{free}}$ . The rate of the spawning events is  $r$  and it is fixed prior to the simulation.

To control the evolution of the ensemble size, we introduce the following parameters: (i) the triplet's unit of weight  $w_u > 0$ , which also fixes the initial number of triplets in the ensemble; (ii) the dead weight  $u_{\text{dw}} > w_u$  which is used throughout the simulation to identify statistically unimportant triplets; and (iii) the spring constant  $\kappa$  of the importance sampling procedure. The triplet's unit of weight  $w_u$  sets a reference to which the number of triplets is evaluated. Thus, in analogy with the definition of the walkers' population in MC

methods, we define the *triplet population*  $P$  as the sum of all the relative absolute value of the weights with respect to  $w_u$ , that is,

$$P = \sum_n \frac{|w_n|}{w_u}. \quad (13)$$

The dead weight and spring constant are approximation and bias parameters, respectively. As such, they are not rooted in the theoretical framework introduced in Sec. II, but they are extra computational features that are necessary for numerical stabilization and convergence. Both the deadweight approximation and importance sampling are discussed in detail in Sec. III B. However, as they are crucial for the execution of the main loop described in this subsection, we briefly recall why they are needed. The deadweight approximation aims to reduce the effect of the dynamical sign problem which is known to cause numerical instabilities connected to fast oscillating exponentials, especially at longer times. Importance sampling reduces the number of triplets needed to obtain a convergent simulation by preventing unwanted extra exploration of the Hilbert space. Thus, the population dynamics is controlled by both  $\kappa$  and  $u_{\text{dw}}$ . In general, if the spring constant is too large, the triplet population decreases quickly. The same being true for the dead weight, both parameters should be optimized. In principle, one should first find the smallest  $u_{\text{dw}}$  that overcomes the dynamical sign problem and, subsequently, decrease the spring constant until a target value of the triplet population is achieved.

We now discuss in detail the main loop of our algorithm, depicted in Fig. 1. The compression and decompression steps are thoroughly described in Appendix.

#### (1) *Spawning*

(a) Preparation to interaction.

(i) Deactivation of unimportant triplets  $(w_n, i_n, j_n)$ . If  $|w_n| < u_{\text{dw}}$ , the triplet becomes inactive and survives with probability  $|w_n|/u_{\text{dw}}$ . The weight of the surviving triplets is updated to  $u_{\text{dw}} w_n / |w_n|$ . The surviving inactive triplets do not experience any collision and are therefore evolved only freely.

(ii) Prespawning decompression. The active triplets are split into  $N_c = \lfloor |w_n|/w_u \rfloor$  child triplets with weight  $w_n/N_c$ .

(b) Spawning. For each child triplet, a side is randomly chosen (quantum mechanically, either  $i_n$  or  $j_n$ ) and a new state  $k_n$  is selected with equal probability among the  $n_t$  possible spawning transitions. For instance, if the ket is chosen, the following triplet is added to the ensemble:

$$\left( i \frac{H_{i_n k_n}^{\text{int}}}{r} \frac{w_n}{N_c} 2n_t T_b, k_n, j_n \right), \quad (14)$$

where  $T_b = e^{\kappa(n_{i_j}^2 - n_{k_j}^2)/2}$  is the transition bias, with  $n_{ij}$  the minimum number of application of  $H^{\text{int}}$  to transition from state  $i$  to  $j$  (see the next subsection for details). If  $j_n$  is selected, an equivalent triplet is spawned on the bra side.

#### (2) *Free evolution*

(a) Full compression. All the child triplets coming from the decompression and the spawnings containing the states  $(i_n, j_n)$  are replaced by a single parent triplet whose weight is the sum of all the slave triplets' weight.

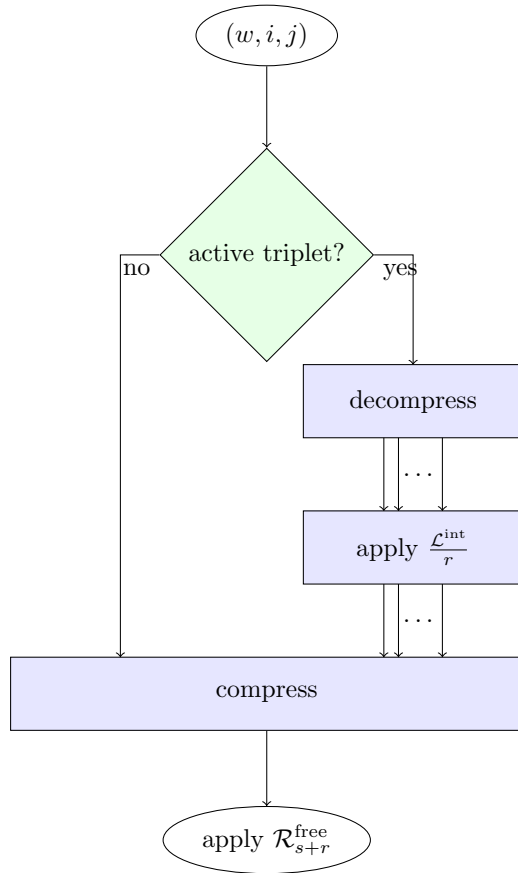


FIG. 1. Flowchart of the algorithm describing the application of the superoperator  $\mathcal{L}^{\text{int}}/r$ . The green diamond represents the deadweight approximation.

(b) Weight update. For each parent triplet  $(w_n, i_n, j_n)$ , a weight update is performed, accounting for the free evolution

$$w_n \mapsto \frac{r}{s + r + i(H_{i_n, i_n}^{\text{free}} - H_{j_n, j_n}^{\text{free}})} w_n. \quad (15)$$

In a typical simulation, correlation functions of the form of Eq. (8) are calculated via a procedure involving an initialization, an iteration on the main loop, and a computation of correlation functions. In the initialization phase, the triplet ensemble is chosen to match the desired initial state  $\rho_0$ . The parameter  $w_u$  uniquely defines the initial population of the ensemble because its normalization is fixed. In this initial ensemble, triplets whose original weight  $w$  is smaller in absolute value than  $w_u$  are either rounded to a weight  $\text{sign}(w)w_u$  with probability  $|w|/w_u$ , or removed completely from the simulation. Subsequently, the main loop is executed  $M_{\text{trunc}}$  times, with the cutoff  $M_{\text{trunc}}$  being set prior to the simulation. At the end of each loop  $m \leq M_{\text{trunc}}$ , the quantity

$$\text{Tr}(AB\tilde{\rho}_s^{(m)}) \quad (16)$$

is calculated and stored, with  $\tilde{\rho}_s^{(m)}$  being the matrix representation of the output of the  $m - 1$  loop. Finally, the correlation function can be computed by summing over all the contribu-

tion from all loops, i.e.,

$$C_s^{AB} \approx \sum_{m=1}^{M_{\text{trunc}}} \text{Tr}(AB\tilde{\rho}_s^{(m)}). \quad (17)$$

Due to the importance sampling procedure, the ensemble is biased by the spring constant  $\kappa$ , and the triplets' weights have to be compensated for to obtain unbiased physical results. For a general operator  $X$ , the physical expectation value is computed using the physical weights  $e^{\frac{\kappa}{2}n_{ij}^2} w_n$  as follows:

$$\text{Tr}(X\tilde{\rho}) \approx \sum_n w_n e^{\frac{\kappa}{2}n_{ij}^2} X_{i_n, j_n}, \quad (18)$$

where  $\tilde{\rho}$  is represented by the ensemble  $\{w_n, i_n, j_n\}_n$  and  $X_{i_n, j_n} = \langle i_n | X | j_n \rangle$ .

## B. Numerical stabilization and convergence

Since most of the computational time is devoted to performing the spawning events, the triplet population introduced in Eq. (13) provides a realistic estimate of the algorithmic complexity. Our simulations show that the computational time scales as  $P_M/s_{\text{min}}$ , where  $P_M$  denotes the maximum triplets' population over all loops. The dependence on the inverse time  $s$  reflects the number of iterations over the main loop that is needed to converge for  $s_{\text{min}} \sim 1/t_{\text{max}}$ . If the initial population is larger, the stability and the accuracy of the results improve, but the simulation time is longer.

The size of a typical many-body Hilbert space imposes a strong demand on the computational resources and limits simulations to small systems. Furthermore, the dynamical sign problem represents a nonnegligible technical issue in terms of numerical stability. To tackle these two problems, we complement the two-process unravelling loop described above with two extra procedures, importance sampling and the deadweight approximation.

The importance sampling procedure relies on two main concepts, originally introduced and explained in detail in Sec. III.C of [47]. The first is the introduction of a *dynamic norm*  $n_{ij}$ , a distance between states in the Hilbert space, defined as the minimum number of applications of  $H^{\text{int}}$  to transition from state  $i$  to  $j$ . The second concept associates to each triplet two weights, a physical weight  $c$  and an ensemble weight  $w$ . The physical weight  $c$  is used to compute expectation values, e.g.,  $\text{Tr}(A\tilde{\rho}_s)$ , whereas the ensemble weight  $w$  reflects the number of jumps performed by the triplet. The latter weight allows to rate the statistical relevance of the triplet within its ensemble without altering the physical averages. These two are related via the equation  $c = bw$ , by a norm-dependent bias  $b \equiv b(n_{ij})$ . A standard choice for  $b$  is  $b = \exp(\frac{\kappa}{2}n_{ij}^2)$ , which is a harmonic interaction with spring constant  $\kappa$  between the states  $i$  and  $j$  that aims at reducing the number of triplets with a large dynamic norm.

The dynamical sign problem manifests itself as numerical instabilities occurring at medium times. To avoid divergences, we need to prevent statistically irrelevant triplet from overcontributing to the dynamics. The basic idea of the deadweight approximation is to forbid all the triplets with an ensemble weight  $w$  below a threshold  $u_{\text{dw}}$  from experiencing jumps

while still allowing them to undergo free evolution. The triplets undergoing the jumps are called active triplets whereas the ones below the threshold  $u_{\text{dw}}$  as referred to as inactive. Intuitively, one can imagine these inactive triplets as an effective environment whose free dynamics is needed to guarantee an ergodic exploration of the Hilbert space by the remaining active triplets.

An extra computational feature which greatly improves the efficiency of the algorithm concerns the parametric nature of  $s$  in the magical formula (5). Unlike time evolution, where typically each iteration at a given physical time  $t' = t + \Delta t$  produces an updated density matrix  $\rho_{t'}$ , the evolution dictated by the magical formula yields results for a density matrix  $\tilde{\rho}_s$  that represents an integral over the entire time range, as reflected in the use of the Laplace transform (3). At first glance, one might be skeptical about the efficiency of our method as one would need to produce an independent simulation for each  $s$  value to reconstruct  $\tilde{\rho}_s$ . However, by noting that the  $s$  variable only appears in the exact free part of the total evolution, one can produce results for the entire  $s$  range in a single simulation at a minimal additional computational cost. For example, two triplets  $(c_m^{(1)}, |\phi_m^{(1)}\rangle, |\psi_m^{(1)}\rangle)$  and  $(c_m^{(2)}, |\phi_m^{(2)}\rangle, |\psi_m^{(2)}\rangle)$  having the very same trajectory for two different values  $s_1 \neq s_2$  differ from one another only in the application of the free evolution operator  $\mathcal{R}_{s+r}^{\text{free}}$ . The idea is then to evolve a single copy of these triplets and reweight each application of the free evolution operator when computing observables simultaneously for  $s_1$  and  $s_2$ . In practice, we select the range of  $s$  values we are interested in before the simulation, and at each iterative order  $m$ , we reweight the triplets for the entire range of  $s$  values during the free evolution part.

#### IV. RESULTS

In this section, we test our algorithm on three models in quantum magnetism, namely the Heisenberg  $XXZ$ , the 1D Ising model, and the 2D square Ising model. In all these scenarios, we look at the dynamics following a quench in some parameter. Although the use of the Laplace transform indicates that the long-term quantities can be naturally computed, we will show that certain time-dependent features can also be reconstructed.

##### A. Heisenberg $XXZ$ model: Analysis of the method and quenched dynamics

To assess the efficiency of our method, we first present a quantitative analysis of our numerical method. In particular, we focus on the triplet population control via the parameters  $w_u$ , and  $u_{\text{dw}}$ , the dependence of the end result on the importance sampling parameter  $\kappa$  and the trace preserving properties of the algorithm.

Like in any Monte Carlo method, the population of walkers is the main quantity responsible for the size of the statistical error bars. Within this method, the population for a given loop refers to the number of spawning attempts during that loop, and due to the high number of spawnings, it naturally increases at an exponential rate. It is therefore vital to slow down any possible overgrowth and limit the exploration of the Hilbert space to statistically important triplets only. In

practice, whenever the target value of the triplets' population is reached, the deadweight approximation is enabled by setting a nonvanishing, fine-tuned threshold  $u_{\text{dw}}$ . This drastically reduces exponential increase in population and further keeps it at a nearly constant value.

To be more concrete we consider the well-known Heisenberg  $XXZ$  model with  $L$  spins and open boundary conditions. Its Hamiltonian reads

$$H = J_{xy} \sum_{i=1}^{L-1} (\sigma_i^x \sigma_{i+1}^x + \sigma_i^y \sigma_{i+1}^y) + J_z \sum_{i=1}^{L-1} \sigma_i^z \sigma_{i+1}^z, \quad (19)$$

where  $\sigma^x, \sigma^z$  are the standard Pauli matrices and the sum runs over the spins in the chain. Following the recipe introduced earlier, the Hamiltonian (19) is split into a free and an interacting part,  $H = H^{\text{free}} + H^{\text{int}}$ , as follows:

$$H^{\text{free}} = J_z \sum_i \sigma_i^z \sigma_{i+1}^z, \quad H^{\text{int}} = J_{xy} \sum_i \sigma_i^+ \sigma_{i+1}^- + \sigma_i^- \sigma_{i+1}^+, \quad (20)$$

where  $\sigma^\pm = \sigma^x \pm i\sigma^y$ . This particular splitting of the Hamiltonian sets the eigenbasis of  $H^{\text{free}}$  as the computational basis, that is,

$$|e_{s_1, \dots, s_L}\rangle = |s_1\rangle \otimes |s_2\rangle \otimes \dots \otimes |s_L\rangle, \quad (21)$$

where  $s_a = s_a^z = \pm 1$ . The single-particle operators  $\sigma^z$  and  $\sigma^\pm$  act on the basis states according to the standard algebra of Pauli matrices

$$\sigma^z |\pm 1\rangle = \pm |\pm 1\rangle, \quad \sigma^\pm |\mp 1\rangle = |\pm 1\rangle, \quad \sigma^\pm |\pm 1\rangle = 0. \quad (22)$$

The initial state is set to

$$\rho_{\text{ini}} = |\text{ini}\rangle \langle \text{ini}|, \quad (23)$$

with

$$|\text{ini}\rangle = \bigotimes_{i=1}^{L/2} | + 1 \rangle_i \bigotimes_{i=L/2+1}^L | - 1 \rangle_i, \quad (24)$$

in which strongly localized spin excitations serve as an initial source of energy. This initial state will be useful later to understand the propagation of spin excitations across the chain.

Figure 2 shows three examples of the evolution of the population and the accuracy of the numerical integration for these populations in the  $L = 10$   $XXZ$  model, for  $J_z = 0.9$ ,  $J_{xy} = 1$ ,  $s = 5 \times 10^{-2}$ ,  $r = 30$ , and  $\kappa = 2$ . In all the examples, the population control is performed by enabling the deadweight approximation at  $m/r = 8$ , represented by the vertical line in the upper panel. The value of the threshold  $u_{\text{dw}}$  then controls the second phase of the exponential increase of the population. In passing, we note that  $w_u$  can be responsible for some secondary effects later during the evolution, e.g., the decreasing distance between the dotted red and dashed orange lines in the first stage in Fig. 2.

The introduction of the importance sampling procedure was motivated by the need to reduce the number of triplets in the ensemble to only the statistically important ones. Thus, the main effect of the  $\kappa$  parameter is a reduction of the number of triplets with a large dynamic norm. A larger  $\kappa$  leads to a

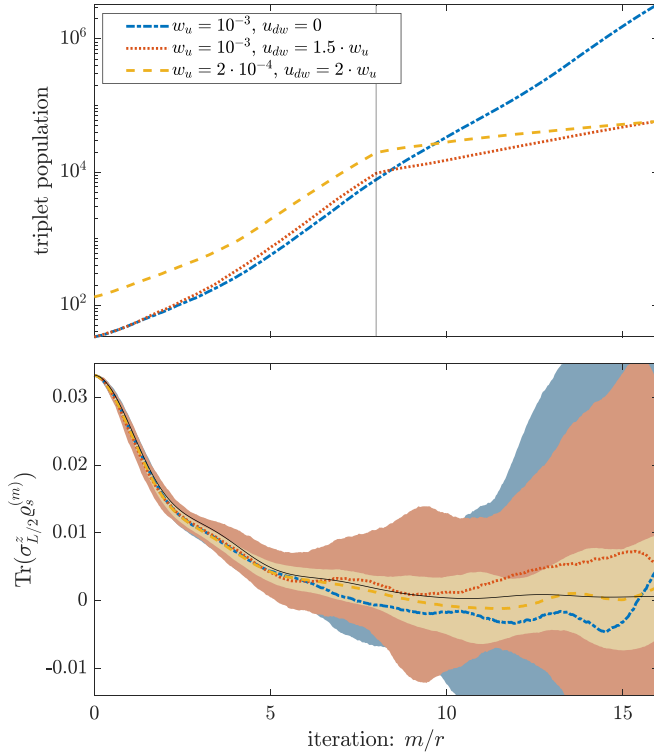


FIG. 2. Upper panel: Evolution of the triplet population for various values of the dead weight  $u_{dw}$  and triplet's unit weight  $w_u$  for the  $L = 10$  XXZ model with  $J_{xy} = 1$ ,  $J_z = 0.9$ ,  $s = 1/20$ ,  $r = 30$ , and  $\kappa = 2$ . The error bars were calculated over 30 independent simulations. Lower panel: Evolution of the quantity  $\text{Tr}(\sigma_{L/2}^z \tilde{\rho}_s^{(m)})$  defined in Eq. (16) for the same parameters as above associated with the magnetization  $\sigma_{L/2}^z$ . The black solid line represents the exact solution.

smaller exponential increase of the population. However, if the spring constant is chosen too large, it may result in a wrong estimate of the final values of the correlation functions (8). This gap originates from breaking the ergodicity of Hilbert space exploration, with the triplets being confined to a small region of the Hilbert space around their initial state. Figure 3 illustrates an underestimation of the quantity  $C_s^{\sigma_{L/2}^z}$

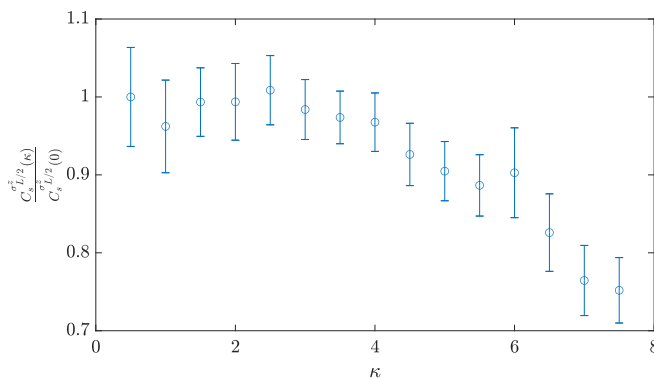


FIG. 3. Dependence of the spring constant  $\kappa$  on the final result  $C_s^{\sigma_{L/2}^z}(\kappa)$  defined in Eq. (8) for a  $L = 8$  XXZ model with  $J_z = 1.5$ ,  $J_{xy} = 1$ , and  $s = 1/10$ . The errors were calculated over 100 independent simulations with  $u_{dw} = 1.125w_u$  and  $r = 30$ .

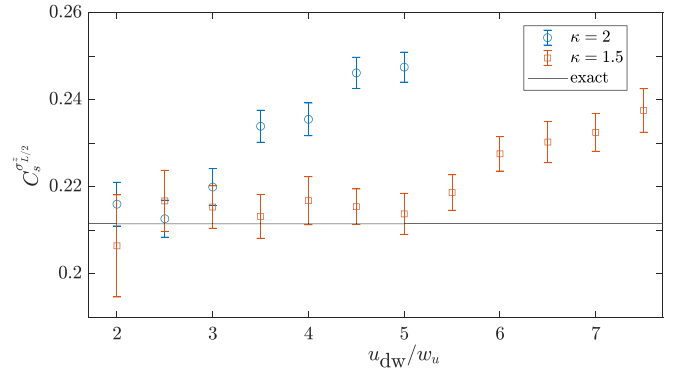


FIG. 4. Estimation of the magnetization  $C_s^{\sigma_{L/2}^z}$  for various dead weight  $u_{dw}$  and various spring constants  $\kappa$ . The model is the  $L = 10$  XXZ, with  $J_z = 0.9$ ,  $J_{xy} = 1$ ,  $s_{\min} = 1/10$ , and  $r = 30$ . The errors were calculated over 100 independent simulations.

in the  $L = 8$  XXZ model with  $J_z = 1.5$ ,  $J_{xy} = 1$  for different values of the spring constant. We note that the importance sampling induces a systematic error for values  $\kappa \geq 4$ , a critical value below which the population is large enough to avoid ergodicity breaking. On a similar note, we remark that the deadweight approximation can also affect the final results. Figure 4 illustrates a  $u_{dw}$  analysis for the  $L = 10$  XXZ model with  $J_z = 0.9$ ,  $J_{xy} = 1$ ,  $s_{\min} = 1/10$ ,  $r = 30$ . The deadweight approximation was enabled at  $m/r = 4$ . Similarly to Fig. 3, we clearly see that if  $u_{dw}$  is chosen too large, the correct result cannot be reached. Lower values of the dead weight  $u_{dw}$  could not be chosen due to divergences related to the sign problem. Figure 4 thus supports the claim that improving the efficiency of the simulation is a trade-off between the parameters  $\kappa$  and  $u_{dw}$ . If the spring constant is too large, the dead weight has to be chosen small, and vice versa. The points  $\kappa = 2$ ,  $u_{dw} = 2.5$  and  $\kappa = 1.5$ ,  $u_{dw} = 5$  are comparable in efficiency, which is supported by similar execution times. To obtain the optimal threshold, it is more efficient to start from a larger value of  $u_{dw}$  and further decrease it until the final result becomes constant within the acceptable statistical error.

The trace conserving character of the evolution operator in the Laplace domain  $\mathcal{R}_s$  can be checked using the following condition [51]:

$$\lim_{s \rightarrow 0} \text{Tr}(\tilde{\rho}_s) = \text{Tr}(\rho_0). \quad (25)$$

If the algorithm violates the unitary character of the time evolution, instabilities will occur and grow exponentially with the simulation length. Figure 5 shows trace conservation according to Eq. (25) with  $\rho_0$  chosen as the ground state of the XXZ Hamiltonian with  $L = 20$ . The exponential growth of the error bars for small  $s$  signals the occurring of the dynamical sign problem. The severity the dynamical sign problem generally depends on the details of the system as well as the observables being computed.

We now focus on the dynamical behavior of spin excitations following an instantaneous quench. For  $J_z < J_{xy}$  these travel ballistically across the chain regardless of its length, while, on the contrary, for  $J_z > J_{xy}$  propagation is inhibited by the strong  $\sigma_z$  coupling [24]. The propagation of these spin excitations can be quantified by analyzing the evolution of

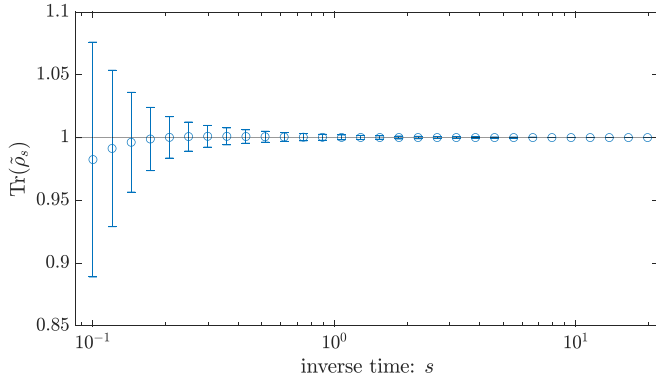


FIG. 5. Evolution of the trace of the density matrix in the Laplace domain  $\tilde{\rho}_s$  for the  $L = 20$  XXZ model with  $J_z = J_{xy} = 1$ . The population was about  $2 \times 10^4$  triplets with  $r = 100$ ,  $\kappa = 4$ ,  $u_{dw} = 1$  at  $m/r = 4$  and the error bars were calculated over 30 independent simulations.

the magnetization profile. Starting from  $\rho_{ini}$ , this profile is calculated as

$$C_s^{\sigma_i^z} \equiv \text{Tr}(\sigma_i^z \tilde{\rho}_s). \quad (26)$$

Figure 6 illustrates the evolution of the absolute value of the magnetization profile (26) for  $J_{xy} = 1$  in both the ballistic and strongly interacting regimes at  $J_z = 0.6$  (top) and  $J_z = 1.5$  (bottom), respectively. In the upper panel, a power-law decay can be observed. This is consistent with ballistic prop-

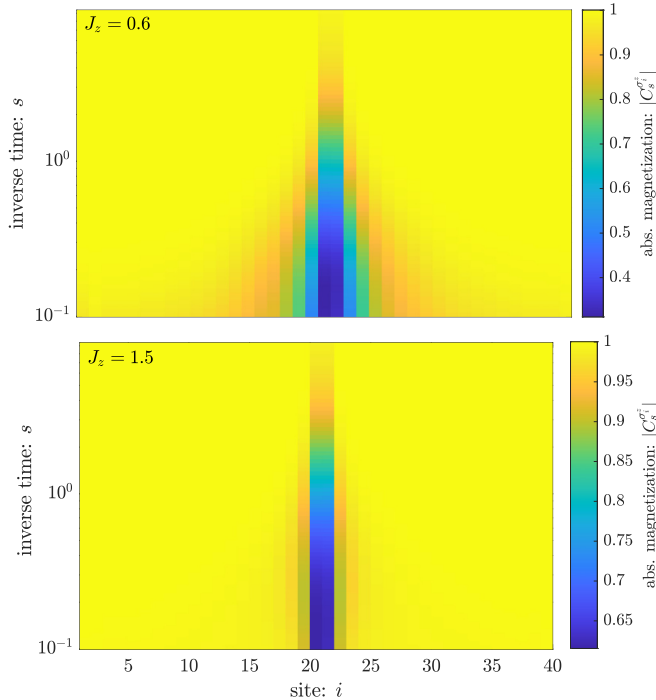


FIG. 6. Evolution in the Laplace domain of the magnetization profile  $|C_s^{\sigma_i^z}|$  for the  $L = 40$  XXZ chain for  $J_{xy} = 1$ . Ballistic behavior is clearly visible in the upper panel, whereas transport is almost completely suppressed in the lower panel. The values plotted were averaged over 100 independent simulations with a population of about  $10^5$  triplets and  $r = 100$ ,  $\kappa = 4$ ,  $u_{dw} = 1$  at  $m/r = 12$ .

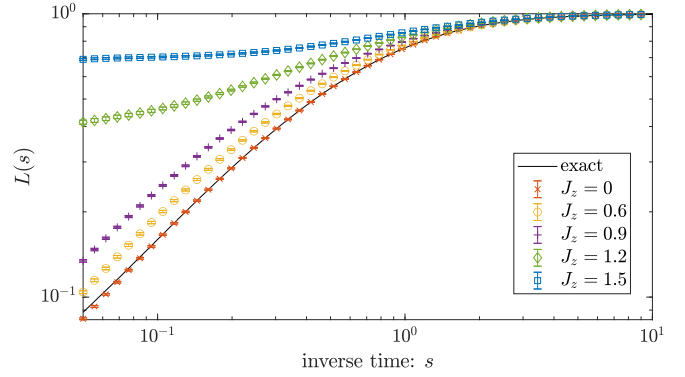


FIG. 7. Evolution of the Loschmidt echo in the Laplace domain  $L(s) = s \text{Tr}(\rho_{ini} \mathcal{R}_s \rho_{ini})$  for the  $L = 40$  XXZ chain with  $J_{xy} = 1$  and various values of  $J_z$ . The errors were estimated over 30 independent simulations, with  $r = 30$ ,  $\kappa = 1$ , and  $u_{dw} = 1.2$  at  $m/r = 12$ . The population at the end of each simulation was about  $2 \times 10^6$  triplets. The continuous curve represents the exact solution for  $J_z = 0$ .

agation where the spin excitations travel within a light-cone type of spatial and temporal region. On the contrary, in the lower panel at  $J_z = 1.5$  magnetization propagation is practically suppressed as a result of the localizing longitudinal interactions. To measure this sharp transition between ballistic and suppressed propagation, we consider the Loschmidt echo  $L(t) = |\langle \psi_0 | e^{-iHt} | \psi_0 \rangle|^2$ , a measure of the disturbance induced on a quantum system by an external perturbation. In the Laplace domain, this reads

$$L(s) = s \text{Tr}(\rho_0 \mathcal{R}_s \rho_0) \equiv \text{Tr}(\rho_0 \tilde{\rho}_s), \quad (27)$$

where  $\rho_0 = |\psi_0\rangle\langle\psi_0|$  is the initial state. Figure 7 illustrates the evolution of  $L(s)$  for  $J_{xy} = 1$  at various  $J_z$  for a spin chain of length  $L = 40$  from the initial state Eq. (23). Increasing  $J_z$  in the Hamiltonian (19) suppresses the propagation of magnetization. The quantum state of the spin chain essentially freezes up as a consequence of strong localization and this results in a weak decay to nearly constant Loschmidt echo. This observation is supported by previous results obtained via exact diagonalization [52].

## B. Confinement in the 1D quantum Ising model

For our second case study, we consider a ferromagnetic quantum Ising chain of length  $L$  coupled to the transverse and longitudinal magnetic fields  $h_x$  and  $h_z$ , respectively. The Hamiltonian reads

$$H = -J \sum_{i=1}^{L-1} \sigma_i^z \sigma_{i+1}^z - h_z \sum_{i=1}^L \sigma_i^z - h_x \sum_{i=1}^L \sigma_i^x, \quad (28)$$

where  $\sigma^x, \sigma^z$  are the standard Pauli matrices and the sum runs over the spins in the chain. In the absence of a longitudinal field, the model is exactly solvable and has a phase transition at  $h_x = J$ . In the ordered phase  $h_x < J$ , the ground state is degenerate due to a spin-flip symmetry breaking and corresponds to domain walls of various lengths. For instance, for  $h_x = h_z = 0$ , the domain walls' lengths are maximized, and the degenerate ground states are  $|\Psi_u\rangle = \bigotimes_{i=1}^L |\uparrow\rangle_i$  and  $|\Psi_d\rangle = \bigotimes_{i=1}^L |\downarrow\rangle_i$ . A nonzero value of the longitudinal field

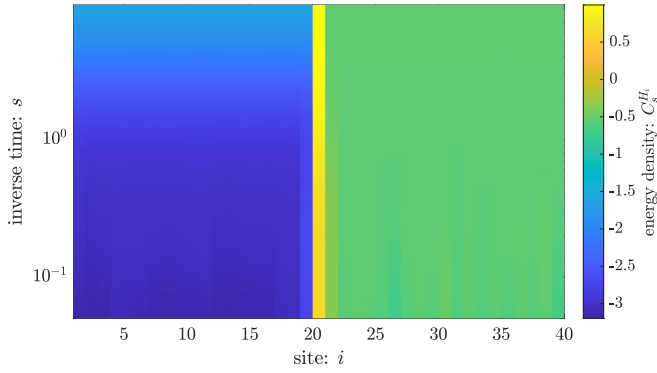


FIG. 8. Evolution in the Laplace domain of the energy density profile  $C_s^{H_i}$  for a  $L = 40$  quantum Ising chain with  $J = 1$ ,  $h_x = 0.2$ , and  $h_z = 1.2$  starting from a state with a single kink in the middle. The profile was computed over 30 independent simulations for  $r = 30$ ,  $\kappa = 3$ , and  $u_{\text{dw}} = 1$  at  $m/r = 6$ .

$h_z$  creates an energy gap between these states by increasing the energy of the spin domains along the field  $h_z$ . Hence, the latter field acts as an attracting potential between the two walls delimiting a domain.

Using our algorithm, we now show how spin dynamics can be suppressed in an Ising chain in the above conditions. Similarly to the  $XXZ$  model studied in the previous subsection, we initialize the evolution of the spin chain from the domain wall state  $|\text{ini}\rangle = |\uparrow \dots \uparrow \downarrow \dots \downarrow\rangle$ . We quench the longitudinal field from  $h_z = 0$  to a nonzero value and study the resulting dynamics. The initial state  $|\text{ini}\rangle$  is characterized by a spin kink exactly in the middle of the chain. Hence, a nonzero longitudinal field will induce an energy imbalance between the two spin domains. Figure 8 shows the evolution in the Laplace domain of the energy density profile  $\text{Tr}(H_i \tilde{\rho}_s)$ , with

$$H_i = -J\sigma_i^z \sigma_{i+1}^z - \frac{h_x}{2}(\sigma_i^x + \sigma_{i+1}^x) - \frac{h_z}{2}(\sigma_i^z + \sigma_{i+1}^z), \quad (29)$$

starting from the initial state Eq. (23) for an  $L = 40$  chain with  $J = 1$ ,  $h_x = 0.2$ , and  $h_z = 1.2$ . Neither energy exchange nor spin excitation propagation occurs between the two halves. This can be explained by considering the mid-kink as a quasiparticle whose motion is triggered by a nonzero longitudinal field  $h_z$ . The kinetic energy gain, which is of order  $\sim h_z$ , allows the kink to move within the potential, but due to energy conservation it has to periodically bounce back, leading to a confined dynamics (see [50] for details). These oscillations are centered around the central bond connecting  $L/2$  and  $L/2 + 1$  and they can be measured by considering the evolution of  $\langle \sigma_{L/2}^z \rangle$ . This is illustrated in the upper panel of Fig. 9 in the Laplace domain for a  $L = 20$  chain with  $J = 1$ ,  $h_x = 0.2$ , and several confining potentials. Because the result is shown in the Laplace domain, the oscillations take the form of Lorentzian curves. The mean frequency of the confining oscillations can be extracted as the inflection point of these curves. This is shown on the lower panel of Fig. 9, which illustrates the logarithmic derivative of the signal in the upper panel. The derivatives were calculated using a cubic spline fitting, and the oscillations frequency is represented by the location of the peak. Furthermore, the oscillation ampli-

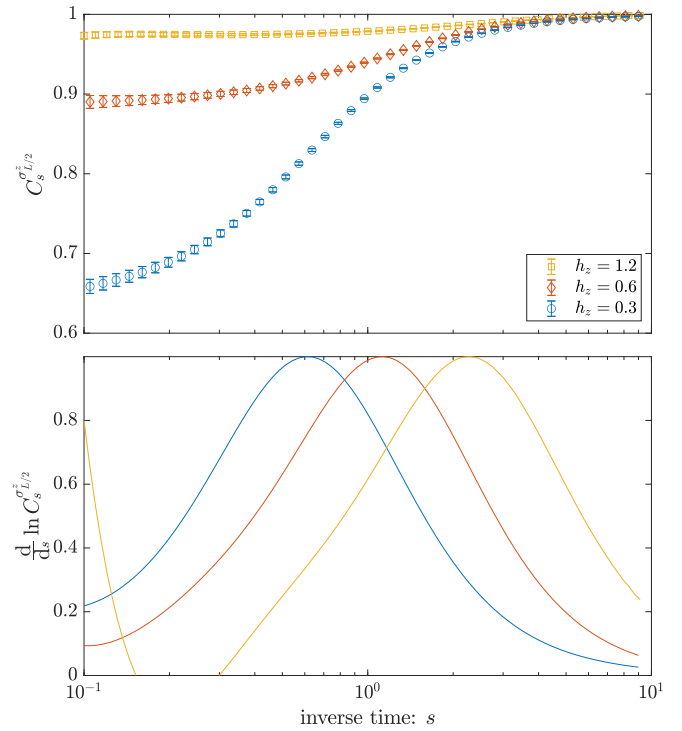


FIG. 9. Upper panel: Evolution in the Laplace domain of the mean magnetization of the spin on the left of the central opposite pair  $C_s^{\sigma_{L/2}^z}$  for the  $L = 20$  quantum Ising chain with  $J = 1$ ,  $h_x = 0.2$  and the parameters  $r = 30$ ,  $\kappa = 2$ , and  $w_u = 4 \times 10^{-6}$ . The deadweight approximation was enabled at  $m/r = 6$  with  $u_{\text{dw}} = 1.6, 1.5, 1.8$  for  $h_z = 1.2, 0.6, 0.3$ , respectively. The choice of specific thresholds  $u_{\text{dw}}$  originates from the optimization procedure. Lower panel: Logarithmic derivative of the magnetization  $C_s^{\sigma_{L/2}^z}$ . The derivative was calculated using a cubic spline fitting.

tudes can be estimated from the distance between the values  $C_{s=0}^{\sigma_{L/2}^z}$  and  $C_{s=\infty}^{\sigma_{L/2}^z}$ . These amplitudes and frequencies scale as  $\sim h_x/h_z$  and  $\sim h_z$ , respectively, which is in agreement with the quasiparticle interpretation of the kink dynamics and with the findings reported in [50]. This is further supported by Fig. 10, which displays the time evolution of the mean value of the magnetization  $\langle \sigma_{L/2}^z \rangle_t$  obtained via an inverse Laplace transform of the data in the upper panel in Fig. 9, using the

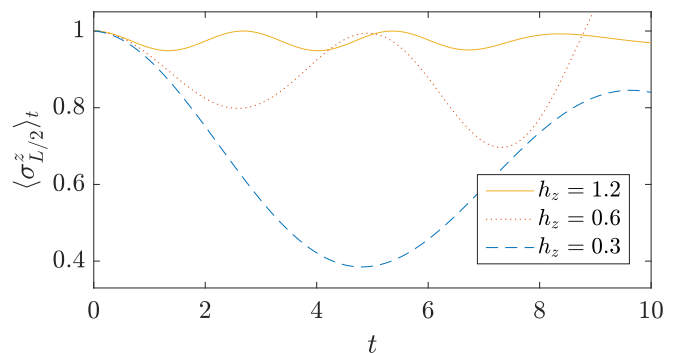


FIG. 10. Time evolution of the magnetization  $\langle \sigma_{L/2}^z \rangle_t$  calculated from an inverse Laplace transform from the data of Fig. 9.

Zakian method. The inverting procedure relies on a rational polynomial fit of the original data to extrapolate the entire Laplace-transformed function. It starts by fitting the signal in Fig. 9 by a function of the type  $P_2/P'_2$  where  $P_2, P'_2$  are polynomials of degree two. The optimal parameters of the first fit are then used as an initial guess for a fit of higher-order polynomials, say  $P_3/P'_3$ . This iterative scheme continues until the parameters start diverging. As illustrated in Fig. 10, the frequency of the oscillations depends linearly on  $h_z$  while the amplitude is inversely proportional. The numerical inverse Laplace method induces numerical amplitude damping due to the use of finite of the  $s$  range. The sharp increase in the magnetization for  $h_z = 0.6$  at about  $t \approx 8$  comes from the dynamical sign problem as well as an interplay between the numerical inverse method and the extrapolation over the entire  $s > 0$  domain, suggesting that the results in the real time domain can be trusted up to  $t \approx 5$ . It is, however, worthy of note that the Laplace signal does not contain any signs of divergences and can hence be trusted at least up to  $s \approx 10$ .

### C. Quenched magnetization dynamics in the 2D Ising model

In this subsection, we briefly show how our method can simulate quantum many-body dynamics in higher dimensions by investigating the magnetization dynamics of a quenched 2D square  $L \times L$  Ising model. In the presence of a transverse field, the Hamiltonian reads

$$H = -J \sum_{\langle i,j \rangle} \sigma_i^z \sigma_j^z - h_x \sum_{i=1}^{L^2} \sigma_i^x, \quad (30)$$

where  $\langle i, j \rangle$  denotes the sum over the nearest neighbors. Similar to the 1D counterpart, this model displays a quantum phase transition from a ferromagnetic to a paramagnetic state with the critical field value being  $h_c = 3.044J$  [53]. We estimate the evolution of the transverse magnetization

$$X = \frac{1}{L^2} \sum_j \sigma_j^x, \quad (31)$$

resulting from a quench of  $h_x$  within the ferromagnetic phase. We choose as the initial state the ground state of the Hamiltonian without transverse field  $h_x = 0$ , that is

$$\rho_0 = |\uparrow \dots \uparrow\rangle \langle \uparrow \dots \uparrow|. \quad (32)$$

Figure 11 illustrates the time evolution of  $X$  for a  $5 \times 5$  Ising model with  $J = 1$  and different field quenches. The data were simulated in the Laplace domain for  $s = 1/2$ ,  $r = 30$ , and  $w_u = 10^{-4}$ . For the fields  $h_x = 0.25$  and  $h_x = 0.5$ , the biases were  $\kappa = 0.2, c_{dw} = 1.2$  and  $\kappa = 0.5, c_{dw} = 1.6$ , respectively, and the deadweight approximation was enabled at  $m/r = 4$ . The Zakian method was then applied to transform the signal to the time domain. These results are in very good agreement with those reported in [53] and demonstrate that our triplet unraveling can provide excellent results in higher dimensions.

Regardless of the dimensionality of the system, the main limitations in our approach are the size of the Hilbert space and the strength of the particle-particle interactions. While the first can be mitigated by increasing the computational resources, the second follows from the expansion of Eq. (5).

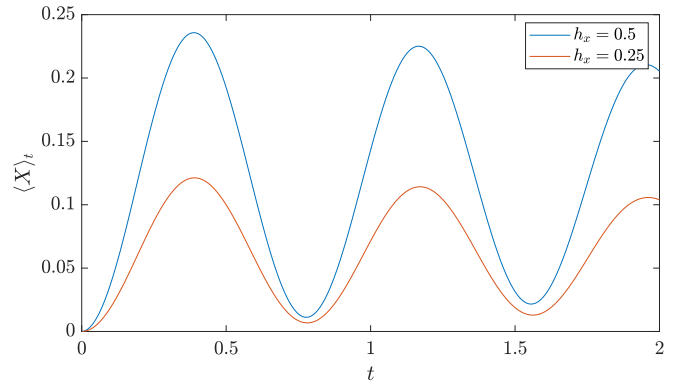


FIG. 11. Time evolution of the total transverse magnetization  $X$  for the  $5 \times 5$  square Ising model with  $J = 1$  starting from the state  $|\uparrow \dots \uparrow\rangle \langle \uparrow \dots \uparrow|$ . This figure illustrates a two-dimensional example where the simulations were performed in the Laplace domain and inverted via the procedure described above. The number of triplets was about  $2 \times 10^5$  whereas the density matrix has approximately  $1.1 \times 10^{15}$  elements.

A quench within the paramagnetic phase was also simulated, leading to a correct asymptotic value of the transverse magnetization  $X$  but with increased numerical noise in the short-time behavior. We suspect that this is associated to the  $\sigma_z$ -to- $\sigma_x$  basis change required by the numerical implementation and, as such, it is the subject of current investigation. As a final remark, we again emphasize that the dependence between the spring constant  $\kappa$  and the deadweight  $c_{dw}$  need to be adjusted to the model under study to obtain a convergent result.

## V. CONCLUSION AND OPEN PERSPECTIVES

In this work, we introduced an alternate Monte Carlo method to study the reversible dynamics of many-body quantum systems. The validity and the accuracy of the method was benchmarked against excitation propagation in the 1D Heisenberg  $XXZ$  model, dynamical confinement in the 1D quantum Ising chain and quench dynamics in the 2D Ising model. In almost all cases, we were able to resolve long-time dynamical properties.

Similarly to FPQMC, this method is based on a piecewise stochastic deterministic two-process unravelling to solve the von Neumann equation. The introduction of an importance sampling procedure allows us to limit the exploration of the Hilbert space to statistically important states. Furthermore, large times can be reached with the deadweight approximation by preventing statistically unimportant triplets from spawning. Due to the unravelling and the form of the evolution operator in the Laplace domain, these triplets can be kept in the simulation by only participating to the free evolution, which greatly reduces the statistical errors on the final result and delays the appearance of the divergences due to the dynamical sign problem. The trace of the density matrix is conserved at all times during the simulation. The maximum simulation time accessible is highly dependent on the observable, as it has been shown between the Loschmidt echo and the oscillations in the quantum Ising model. Unfortunately, we doubt that larger timescales can be reached.

Regarding future directions, we believe that the introduction of a small dissipation parameter can reduce the severity of the sign problem, an idea that is already under current investigation. Thus, we are confident that our method can be extended to dissipative many-body quantum systems.

#### APPENDIX: COMPRESSION AND DECOMPRESSION STEPS

Prior to the execution of the loop the ensemble is modified as to improve the statistics without influencing directly the averages. This modification is carried out through *compressions* or *decompressions*.

In a compression, classes of triplets are formed by grouping together all the triplets associated to a fixed pair of states, for instance,  $(i, j)$ . These are then replaced by a single triplet whose weight is equal to the sum of the weights of all the members of the class.

Decompression is applied on a compressed ensemble. A single class of triplets  $(i, j)$  is split into triplets with weight  $w_u > 0$  in absolute value,  $(\text{sgn}(w_n)w_n, i_n, j_n)$ , and a single rest triplet  $(w_r, i_n, j_n)$ , with  $w_r = \text{sgn}(w_n)(|w_n/w_u| - \lfloor |w_n/w_u| \rfloor)$  ( $\lfloor \cdot \rfloor$  is the floor function). The rest triplet is then removed from the simulation with probability  $1 - |w_r|$ ; otherwise its weight is updated to  $\text{sgn}(w_n)w_u$ . That way, the total statistical weight is conserved on average.

- 
- [1] J. Eisert, M. Friesdorf, and C. Gogolin, Quantum many-body systems out of equilibrium, *Nat. Phys.* **11**, 124 (2015).
- [2] B. Lake, A. M. Tsvelik, S. Notbohm, D. Alan Tennant, T. G. Perring, M. Reehuis, C. Sekar, G. Krabbes, and B. Büchner, Confinement of fractional quantum number particles in a condensed-matter system, *Nat. Phys.* **6**, 50 (2010).
- [3] S. Hild, T. Fukuhara, P. Schauß, J. Zeiher, M. Knap, E. Demler, I. Bloch, and C. Gross, Far-From-Equilibrium Spin Transport in Heisenberg Quantum Magnets, *Phys. Rev. Lett.* **113**, 147205 (2014).
- [4] J. P. Ronzheimer, M. Schreiber, S. Braun, S. S. Hodgman, S. Langer, I. P. McCulloch, F. Heidrich-Meisner, I. Bloch, and U. Schneider, Expansion Dynamics of Interacting Bosons in Homogeneous Lattices in One and Two Dimensions, *Phys. Rev. Lett.* **110**, 205301 (2013).
- [5] I. Bloch, J. Dalibard, and S. Nascimbène, Quantum simulations with ultracold quantum gases, *Nat. Phys.* **8**, 267 (2012).
- [6] C. Gross and I. Bloch, Quantum simulations with ultracold atoms in optical lattices, *Science* **357**, 995 (2017).
- [7] F. Schäfer, T. Fukuhara, S. Sugawa, Y. Takasu, and Y. Takahashi, Tools for quantum simulation with ultracold atoms in optical lattices, *Nat. Rev. Phys.* **2**, 411 (2020).
- [8] R. Blatt and C. F. Roos, Quantum simulations with trapped ions, *Nat. Phys.* **8**, 277 (2012).
- [9] C. Monroe, W. C. Campbell, L.-M. Duan, Z.-X. Gong, A. V. Gorshkov, P. W. Hess, R. Islam, K. Kim, N. M. Linke, G. Pagano, P. Richerme, C. Senko, and N. Y. Yao, Programmable quantum simulations of spin systems with trapped ions, *Rev. Mod. Phys.* **93**, 025001 (2021).
- [10] G. Romero, E. Solano, and L. Lamata, in *Quantum Simulations with Circuit Quantum Electrodynamics*, edited by D. G. Angelakis (Springer International Publishing, New York, 2017).
- [11] A. Petrescu, H. E. Türeci, A. V. Ustinov, and I. M. Pop, Fluxon-based quantum simulation in circuit QED, *Phys. Rev. B* **98**, 174505 (2018).
- [12] L. D'Alessio, Y. Kafri, A. Polkovnikov, and M. Rigol, From quantum chaos and eigenstate thermalization to statistical mechanics and thermodynamics, *Adv. Phys.* **65**, 239 (2016).
- [13] F. Alet and N. Laflorencie, Many-body localization: An introduction and selected topics, *C. R. Phys.* **19**, 498 (2018).
- [14] J. M. Deutsch, Eigenstate thermalization hypothesis, *Rep. Prog. Phys.* **81**, 082001 (2018).
- [15] M. Cheneau, P. Barmettler, D. Poletti, M. Endres, P. Schauß, T. Fukuhara, C. Gross, I. Bloch, C. Kollath, and S. Kuhr, Light-cone-like spreading of correlations in a quantum many-body system, *Nature (London)* **481**, 484 (2012).
- [16] R. Geiger, T. Langen, I. E. Mazets, and J. Schmiedmayer, Local relaxation and light-cone-like propagation of correlations in a trapped one-dimensional bose gas, *New J. Phys.* **16**, 053034 (2014).
- [17] J. Faupin, M. Lemm, and I. M. Sigal, Maximal Speed for Macroscopic Particle Transport in the Bose-Hubbard Model, *Phys. Rev. Lett.* **128**, 150602 (2022).
- [18] E. Canovi, P. Werner, and M. Eckstein, First-Order Dynamical Phase Transitions, *Phys. Rev. Lett.* **113**, 265702 (2014).
- [19] M. Heyl, Dynamical quantum phase transitions: A brief survey, *Europhys. Lett.* **125**, 26001 (2019).
- [20] V. Link and W. T. Strunz, Dynamical Phase Transitions in Dissipative Quantum Dynamics with Quantum Optical Realization, *Phys. Rev. Lett.* **125**, 143602 (2020).
- [21] A. Polkovnikov, K. Sengupta, A. Silva, and M. Vengalattore, Colloquium: Nonequilibrium dynamics of closed interacting quantum systems, *Rev. Mod. Phys.* **83**, 863 (2011).
- [22] R. Nandkishore and D. A. Huse, Many-body localization and thermalization in quantum statistical mechanics, *Annu. Rev. Condens. Matter Phys.* **6**, 15 (2015).
- [23] B. Bertini, F. Heidrich-Meisner, C. Karrasch, T. Prosen, R. Steinigeweg, and M. Žnidarič, Finite-temperature transport in one-dimensional quantum lattice models, *Rev. Mod. Phys.* **93**, 025003 (2021).
- [24] D. Gobert, C. Kollath, U. Schollwöck, and G. Schütz, Real-time dynamics in spin- $\frac{1}{2}$  chains with adaptive time-dependent density matrix renormalization group, *Phys. Rev. E* **71**, 036102 (2005).
- [25] J. Sirker, R. G. Pereira, and I. Affleck, Diffusion and Ballistic Transport in One-Dimensional Quantum Systems, *Phys. Rev. Lett.* **103**, 216602 (2009).
- [26] K. A. Al-Hassanieh, A. E. Feiguin, J. A. Riera, C. A. Büsser, and E. Dagotto, Adaptive time-dependent density-matrix renormalization-group technique for calculating the conductance of strongly correlated nanostructures, *Phys. Rev. B* **73**, 195304 (2006).
- [27] H. Aoki, N. Tsuji, M. Eckstein, M. Kollar, T. Oka, and P. Werner, Nonequilibrium dynamical mean-field theory and its applications, *Rev. Mod. Phys.* **86**, 779 (2014).

- [28] D. Lacroix and S. Ayik, Stochastic quantum dynamics beyond mean field, *Eur. Phys. J. A* **50**, 95 (2014).
- [29] Q. Dong, I. Krivenko, J. Kleinhenz, A. E. Antipov, G. Cohen, and E. Gull, Quantum Monte Carlo solution of the dynamical mean field equations in real time, *Phys. Rev. B* **96**, 155126 (2017).
- [30] Y. Mizuno, K. Tsutsui, T. Tohyama, and S. Maekawa, Nonlinear optical response and spin-charge separation in one-dimensional mott insulators, *Phys. Rev. B* **62**, R4769(R) (2000).
- [31] A. Amaricci, C. Weber, M. Capone, and G. Kotliar, Approach to a stationary state in a driven Hubbard model coupled to a thermostat, *Phys. Rev. B* **86**, 085110 (2012).
- [32] M. Eckstein, M. Kollar, and P. Werner, Thermalization After an Interaction Quench in the Hubbard Model, *Phys. Rev. Lett.* **103**, 056403 (2009).
- [33] M. Eckstein and M. Kollar, Nonthermal Steady States After an Interaction Quench in the Falicov-Kimball Model, *Phys. Rev. Lett.* **100**, 120404 (2008).
- [34] M. Eckstein and M. Kollar, Near-adiabatic parameter changes in correlated systems: Influence of the ramp protocol on the excitation energy, *New J. Phys.* **12**, 055012 (2010).
- [35] A. D. McLachlan and M. A. Ball, Time-dependent Hartree-Fock theory for molecules, *Rev. Mod. Phys.* **36**, 844 (1964).
- [36] M. Nest, T. Klamroth, and P. Saalfrank, The multiconfiguration time-dependent Hartree-Fock method for quantum chemical calculations, *J. Chem. Phys.* **122**, 124102 (2005).
- [37] R. O. Jones, Density functional theory: Its origins, rise to prominence, and future, *Rev. Mod. Phys.* **87**, 897 (2015).
- [38] L. Mühlbacher and E. Rabani, Real-Time Path Integral Approach to Nonequilibrium Many-Body Quantum Systems, *Phys. Rev. Lett.* **100**, 176403 (2008).
- [39] K. Guther, W. Dobrautz, O. Gunnarsson, and A. Alavi, Time Propagation and Spectroscopy of Fermionic Systems Using a Stochastic Technique, *Phys. Rev. Lett.* **121**, 056401 (2018).
- [40] P. Werner, T. Oka, and A. J. Millis, Diagrammatic Monte Carlo simulation of nonequilibrium systems, *Phys. Rev. B* **79**, 035320 (2009).
- [41] M. S. Church and B. M. Rubenstein, Real-time dynamics of strongly correlated fermions using auxiliary field quantum Monte Carlo, *J. Chem. Phys.* **154**, 184103 (2021).
- [42] F. Goth and F. F. Assaad, Time and spatially resolved quench of the fermionic Hubbard model showing restricted equilibration, *Phys. Rev. B* **85**, 085129 (2012).
- [43] A. Alexandru, G. Başar, P. F. Bedaque, S. Vartak, and N. C. Warrington, Monte Carlo Study of Real Time Dynamics on the Lattice, *Phys. Rev. Lett.* **117**, 081602 (2016).
- [44] M. Schiró and M. Fabrizio, Real-time diagrammatic Monte Carlo for nonequilibrium quantum transport, *Phys. Rev. B* **79**, 153302 (2009).
- [45] E. Gull, D. R. Reichman, and A. J. Millis, Numerically exact long-time behavior of nonequilibrium quantum impurity models, *Phys. Rev. B* **84**, 085134 (2011).
- [46] G. Cohen, E. Gull, D. R. Reichman, and A. J. Millis, Taming The Dynamical Sign Problem in Real-Time Evolution of Quantum Many-Body Problems, *Phys. Rev. Lett.* **115**, 266802 (2015).
- [47] R. Chessex, M. Borrelli, and H. C. Öttinger, Fixed-point quantum monte carlo method: A combination of density-matrix quantum monte carlo method and stochastic unravellings, *Phys. Rev. A* **105**, 062803 (2022).
- [48] M. Kormos, M. Collura, G. Takács, and P. Calabrese, Real-time confinement following a quantum quench to a non-integrable model, *Nat. Phys.* **13**, 246 (2017).
- [49] R. Verdel, F. Liu, S. Whitsitt, A. V. Gorshkov, and M. Heyl, Real-time dynamics of string breaking in quantum spin chains, *Phys. Rev. B* **102**, 014308 (2020).
- [50] P. P. Mazza, G. Perfetto, A. Lerose, M. Collura, and A. Gambassi, Suppression of transport in nondisordered quantum spin chains due to confined excitations, *Phys. Rev. B* **99**, 180302(R) (2019).
- [51] H. C. Öttinger, *A Philosophical Approach to Quantum Field Theory* (Cambridge University Press, Cambridge, England, 2017).
- [52] J. Viti, J.-M. Stéphan, J. Dubail, and M. Haque, Inhomogeneous quenches in a free fermionic chain: Exact results, *Europhys. Lett.* **115**, 40011 (2016).
- [53] J. Richter, T. Heitmann, and R. Steinigeweg, Quantum quench dynamics in the transverse-field Ising model: A numerical expansion in linked rectangular clusters, *SciPost Phys.* **9**, 031 (2020).